PAPER

New insight into strain and composition of BaZrO₃ nanorods in REBCO superconductor

To cite this article: Goran Majkic et al 2021 Supercond. Sci. Technol. 34 115002

View the article online for updates and enhancements.

You may also like

- Critical current density of YBa2Cu2Ofilms with BaZrO₃ inclusions on SrTiO₃ A Augieri, V Galluzzi, G Celentano et al.
- High critical current density over 1 MA cm² at 13 T in BaZrO₂ incorporated Ba(Fe,Co)₂As₂ thin film Jongmin Lee, Jianyi Jiang, Fumitake Kametani et al.
- Comparison study of the flux pinning enhancement of YBCO superconductor with BZO and BZO + Y2O3 mixed phase

M A Sebastian, C Ebbing, W Zhang et al.



IOP ebooks™

Bringing together innovative digital publishing with leading authors from the global scientific community.

Start exploring the collection-download the first chapter of every title for free.

Supercond. Sci. Technol. 34 (2021) 115002 (13pp)

https://doi.org/10.1088/1361-6668/ac23ba

New insight into strain and composition of BaZrO₃ nanorods in REBCO superconductor

Goran Majkic^{1,*}, Jong Seok Jeong², Hwanhui Yun², Francisco C Robles Hernandez³, Eduard Galstyan¹, Rudra Pratap¹, Huikai Cheng⁴, Adam Stokes⁴, K Andre Mkhoyan² and Venkat Selvamanickam¹

E-mail: gmajkic@uh.edu

Received 1 May 2021, revised 25 August 2021 Accepted for publication 3 September 2021 Published 28 September 2021



Abstract

We report on strain and composition effects associated with growth of self-assembled BaZrO₃ (BZO) nanorods in REBa₂Cu₃O_{7- δ} (REBCO) superconductors (RE = rare earth = Y and Gd), which have a profound effect on flux pinning and in-field critical current performance. The *a-b* plane mismatch between BZO and REBCO is never fully coherently accommodated. Instead, the nanorods always assume a size at least one unit cell smaller than the corresponding 'hole' in the REBCO matrix, thus providing deep minima of in-plane mismatch strain. Next, we show that the nominal BZO nanorods are in fact solid solution Ba²⁺(Zr⁴⁺_{1-z}RE³⁺_z)O_{3- δ} perovskite, thus strongly affecting the stoichiometry and relative amounts of REBCO and BZO. We demonstrate that by varying only the Ba content in the nominal composition of 15 mol.% BZO + REBCO, the unit cell density of BZO can be tuned from 5% to 23%, and the linear density of RE₂O₃ (REO) precipitates from 18 to 1 μ m⁻¹. The results explain the wide range of pinning performances observed for the same nominal amount of Zr addition and provide insight into the mechanisms behind the complex phenomenon of growth of nanorods by self-assembly in REBCO superconductors.

Keywords: 2G-HTS, YBCO, REBCO, superconductor, BZO, nanorods, TEM

(Some figures may appear in colour only in the online journal)

1. Introduction

The discovery of growth of BaZrO₃ (BZO) nanorods by self-assembly in the REBa₂Cu₃O_{7- δ} (REBCO, RE = rare earth = Y and Gd) superconductors has had a profound impact on their in-field performance [1–10]. The nanorods grow

along the crystallographic c-axis direction of REBCO with diameters comparable to the coherence length (\sim 4–10 nm), [11–16] which act as directional pinning centers that drastically increase the pinning force under applied magnetic field. Multiple systems of the general form BaMO₃ (M = Hf, Sn, Ti, Nb, Ce, etc) have since been discovered to result in growth of nanorods [2, 17–33], with a common characteristic of all of them being ABO₃-type perovskites containing Ba on the A-site. Additionally, excess RE readily

¹ Department of Mechanical Engineering, Advanced Manufacturing Institute, Texas Center for Superconductivity, University of Houston, Houston, TX 77204, United States of America

² Department of Chemical Engineering and Materials Science, University of Minnesota, Minneapolis, MN 55455, United States of America

³ Department of Mechanical Engineering Technology, Advanced Manufacturing Institute, University of Houston, Houston TX 77204, United States of America

⁴ Thermo Fisher Scientific, NanoPort-Portland, 5350 NE Dawson Creek Drive, Hillsboro, OR 97124, United States of America

^{*} Author to whom any correspondence should be addressed.

forms 'spherical' or isotropically shaped RE_2O_3 (REO) precipitates epitaxially oriented as REO(220)||REBCO(100), REO(004)||REBCO(001) [34], which further contribute to isotropic pinning.

The striking effect of nanorods on flux pinning has sparked intense research on in-field performance optimization and mechanisms of self-assembly, including strain mismatch, growth kinetics and other aspects [5, 15, 17–23, 35–61]. The studies report widely varying nanorod landscapes, matching field, crystallographic texture, lattice parameters, critical temperature (T_c) , self-field and in-field critical current (I_c) , angular in-field I_c dependence, size and density of nanorods, their angular splay distribution, and other relevant parameters [1, 9, 13, 15, 19, 22, 41, 42, 48, 51, 61–73]. The level of improvement of in-field performance has been significant, with drastic increase in performance over a wide range of operating regimes, e.g. 30 K-50 K, 3-5 T and 4.2 K, up to 31.2 T [1, 3, 5]. Our reported critical current performance at 4.2 K, 15 T, Bllc-axis is a factor of 2.5–5 higher than any other available 4.2 K superconductor technology or material system at present [1, 3, 74].

Several attempts have been made to explain the driving force behind their 1D oriented growth and predict the equilibrium nanorod diameter and areal density [40, 43, 75]. The effect of elastic (or coherent) mismatch strain has been used to analyze the effect on equilibrium diameter [75] and morphology of BZO [16]. Strain decay modes have also been considered, as well as the interfacial energy by introducing energy terms to represent non-coherent interfacial energy along the *c*-axis direction in a phenomenological way [40]. The in-plane, or *a-b* plane mismatch strain, has always been assumed to be coherently accommodated. In contrast to out-of-plane mismatch studies, information on in-plane or *a-b* plane mismatch accommodation mechanisms is scarce. We do note one report where in-plane strain accommodation via dislocations was shown for one nanorod [11].

In this manuscript, we present results and findings from plane-view aberration-corrected scanning transmission electron microscopy (Cs-STEM) combined with energy dispersive x-ray spectroscopy (EDS) and conventional TEM studies of the BZO/REBCO system. The analysis of the mechanisms of strain accommodation as well as elemental composition at the BZO/REBCO interfaces shows that: (a) the nanorods are never coherently accommodated along the a-b plane, but instead, spontaneously grow at least one unit cell smaller than the REBCO host matrix, (b) the believed stoichiometric BaZrO₃ composition is in fact a solid solution $Ba^{2+}(Zr^{4+}_{1-x}RE^{3+}_{x})O_{3-\delta}$ with implications on the composition of host REBCO and REO, and on the elastic mismatch strain energy [75, 76], and finally (c) dramatic changes in relative amounts of BZO and REO can be achieved by controlling only Ba non-stoichiometry.

2. Experimental

All REBCO/BZO samples have been grown on flexible hastelloy substrates capped with a buffer layer consisting of

Al₂O₃/Y₂O₃/IBAD-MgO/homo-epi MgO/LaMnO₃ film stack [77, 78]. The films have been deposited using the newly developed advanced metal-organic chemical vapor deposition (A-MOCVD), system that enables growth of very thick films (up to 5 μ m) of high texture quality throughout the thickness [1, 3, 5, 13, 60, 79]. Metal-tetra methylheptanedionate precursors have been used with tetrahydrofuran as a solvent.

The composition of the deposited films was determined using inductively coupled plasma—mass spectroscopy. For each measurement, the instrument was calibrated using an appropriate standard containing all elements of interests. 2D-XRD analysis has been implemented using a Bruker D8 Discover instrument equipped with a Vantec 500 Detector at a working distance of 20 cm. A microfocus Cu source with integrated Montel optics and 0.5 mm double pin collimator were used in this study.

The plane view TEM samples were prepared by mechanical dimpling followed by 5 keV dual beam Ar ion milling at 7° inclination relative to the surface. The cross-section samples were prepared using focused ion beam, followed by low energy Ar beam cleaning and final thinning. Both plane-view and cross-section coupons were prepared from the same samples from nearby areas. The Cs-STEM study has been conducted using FEI Titan G2 60-300 (S)TEM equipped with a CEOS DCOR probe corrector, a Schottky extreme field emission gun, and a monochromator. The STEM images presented here are recorded using high-angle annular darkfield (HAADF) detector. STEM-EDS data were collected by a super-X energy dispersive x-ray detector. Care was taken to distinguish between edges with closely spaced energies such as Y and Zr K edges. Conventional amplitude/diffraction contrast TEM analysis has been performed on a JEOL 2000FX.

Selective Bragg-filtering was performed on HAADF images by incorporating all peaks of interest and crosscomparing original and filtered images to ensure that all features of interest are preserved and no artifacts introduced. Geometric Phase Analysis (GPA) and nearest-neighbor grid Search were performed using custom-developed algorithms and executed in Matlab. For GPA, strain-free reference regions were selected in the REBCO matrix, as indicated with the red rectangle shown in figure 1. Both direct [80] and Fourier space strain calculations [81] have been implemented and crosscompared to ensure consistency of the results. Phase optimization relative to the reference crystal has been implemented utilizing non-linear optimization, yielding sub-pixel resolution. Peak-Pair or nearest-neighbor search was performed using a constrained nearest neighbor search on a predefined grid (e.g. [100]/[010]), followed by Voronoi/Delaunay segmentation, intensity integration and peak identification based on target column and neighboring column intensities. Both 2D ellipse fit and peak value location methods have been used and cross-compared to check for consistency.

For statistical analysis or nanorod size and distribution, conventional amplitude/diffraction contrast TEM imaging was used. This approach was chosen in order to readily obtain a large enough statistical dataset, at the expense of some spatial resolution compared to HAADF images. The BZO nanorods and REO nano-precipitates are readily identifiable in the

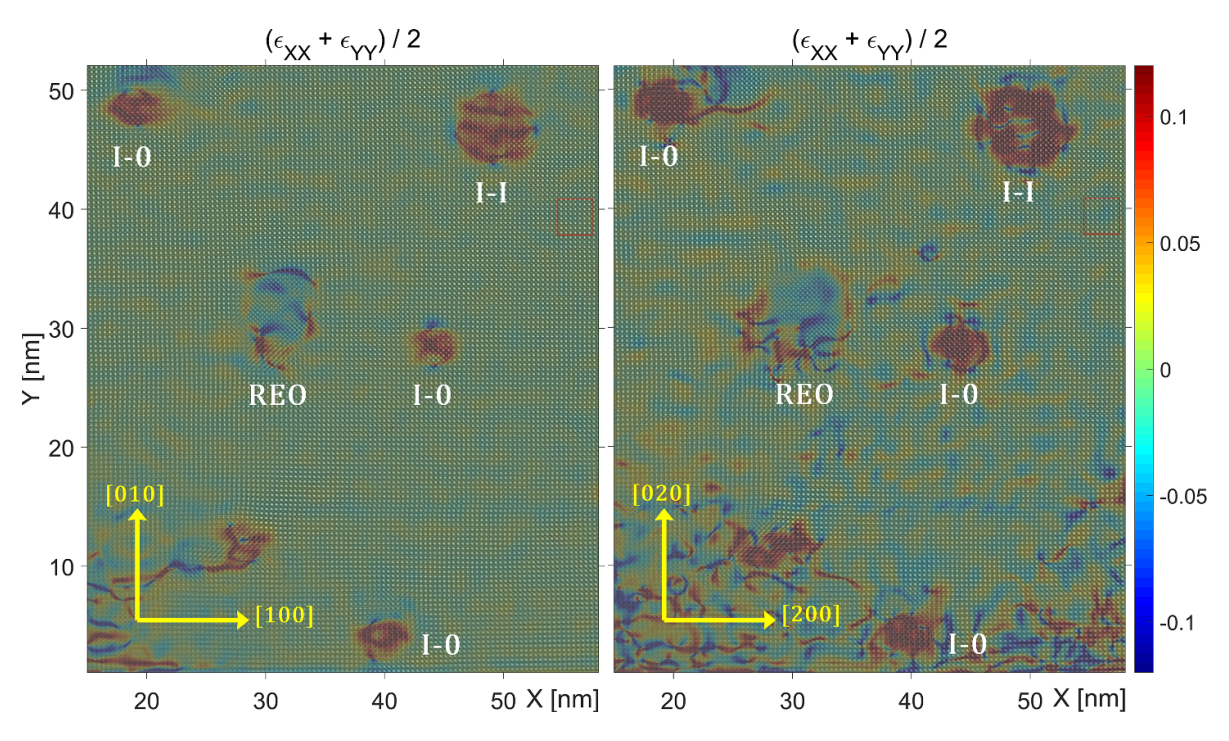


Figure 1. Plane-view HAADF image of REBCO containing $BaZrO_3$ and RE_2O_3 . The colormaps represent dilatational 'strain' from GPA analysis based on (a) 100/010 and (b) 200/020 reflections. The singularities at the REBCO/BZO interfaces represent (a) 'antiphase' locations and (b) dislocations, and only the 200/020 based map represents true measures of strain. Two types of BZO have been identified: I-0 and I-I, based on the number of antiphase lines along [100]-[010] directions.

images due to the typically strong contrast obtained using this technique. Care was taken in measuring nanorod size to measure the correct cross section and avoid the artifacts occurring from inclined nanorods that in plane-view micrographs appear as elongated shapes. The identified nanorod center coordinates were subjected to Delaunay triangulation and Voronoi cell segmentation for determining the distribution of nanorod spacing and area occupied per nanorod.

3. Results and discussion

In this study, all films contained nominal 15 mol.% addition of Zr and 30 mol.% RE excess, for nominal unit cell content of 1 REBCO: 0.15 BZO:0.15 REO. The examined samples differed in the amount of Ba relative to the nominally stoichiometric or 'fully compensated' Ba/Cu ratio of 2.15/3. For the samples used in this study, the Ba content was varied from under- to over-compensated, i.e. from Ba/Cu < 2.15/3 to >2.15/3.

In the following, we present the composition as (Ba + Zr)/Cu ratio, for the reasons of the previously found strong correlation of in-field performance and other characteristics with this metric, as well as for easy cross-comparisons [15, 48, 61]. The fully compensated case corresponds to (Ba + Zr)/Cu = (2.15 + 0.15)/3 = 0.767, and the examined samples can be thought of as samples centered around nominal composition of $RE_{1.3}Ba_{2+x}Cu_3 + 0.15$ Zr, with variation in Ba excess/deficiency content, x.

3.1. In-plane strain accommodation

Shown in figure 1 is a plane view CS-TEM micrograph of a region containing BZO nanorods embedded in the REBCO matrix, as well as a RE₂O₃ precipitate. Superimposed are the color maps of in-plane dilatation $(\varepsilon_{11} + \varepsilon_{22})/2$ obtained from geometric phase analysis (GPA) [80], based on (100) and (200) reflections. While only the analysis based on the (200) reflections should be interpreted as strain, the maps based on the (100) reflections readily expose the singularities at the BZO/REBCO interfaces where REBCO and BZO unit cells are exactly out of phase, which we call 'antiphase' lines. For each missing unit cell in BZO, one antiphase is formed. We classify the nanorods shown in figure 1 as I-0 and I-I type, where 'I' or '0' denote the difference between the number of unit cells of REBCO and BZO along [100] and [010] directions, respectively. For example, the I-0 type is coherently bonded in one direction and has one BZO unit cell missing in the perpendicular direction. The analysis of the dilatation strain based on (200) reflections show that for one antiphase line two edge dislocations form near-symmetrically around it. Out of more than 50 BZO particles analyzed on six different samples, not a single fully coherent/elastic 0-0 type BZO nanorod has been detected. Instead, all analyzed particles were exclusively either of I-0 or I-I type. One exception is the presence of 'bottleshape' BZO with modulation in size, where the nanorods modulate in size along the c-axis from I-0/I-I type to II-II type and back to I-0/I-I type, as will be presented.

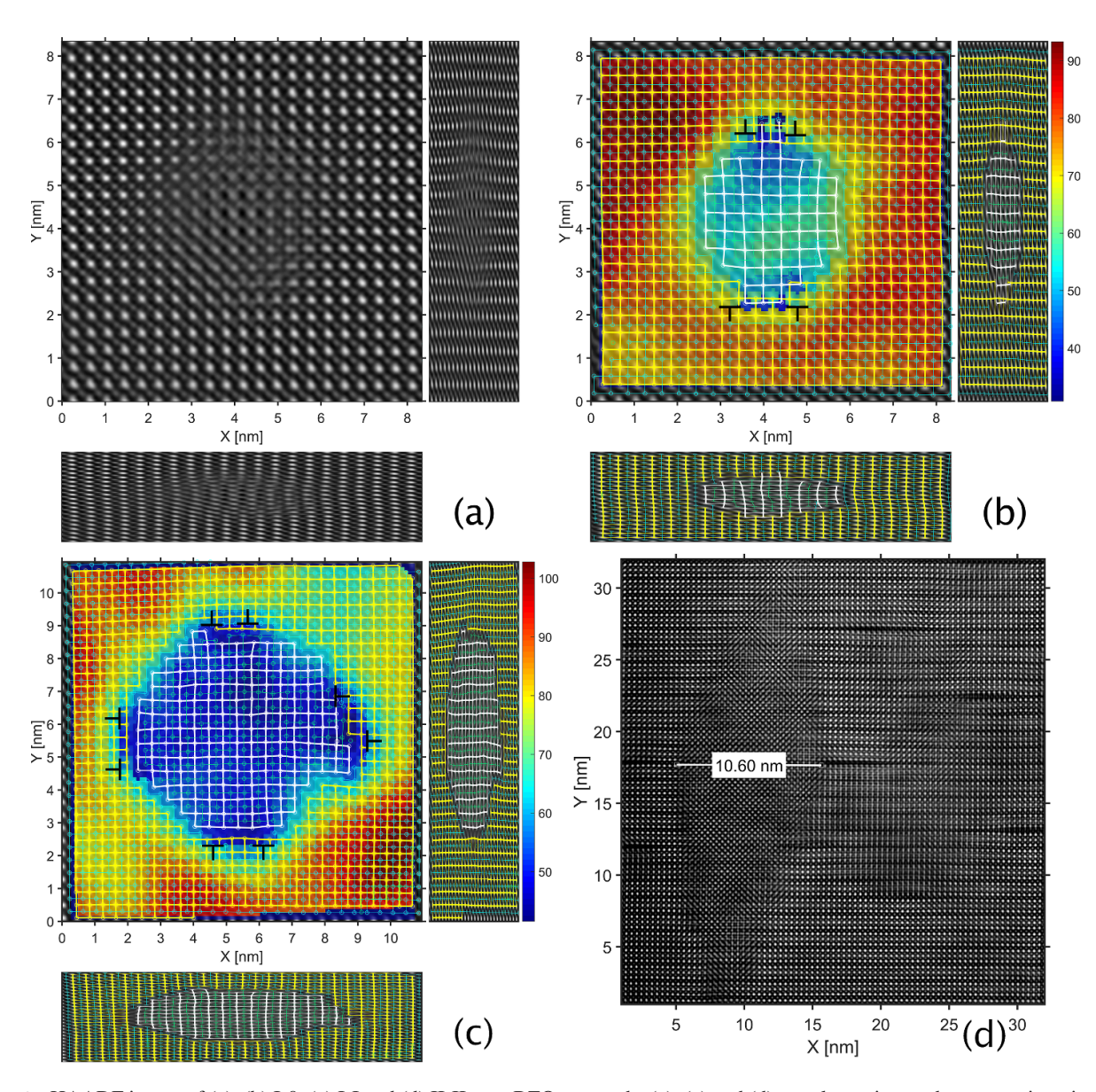


Figure 2. HAADF image of (a), (b) I-0, (c) I-I and (d) II-II type BZO nanorods. (a)–(c) and (d) are plane-view and cross section views, respectively. The colormaps and dots/grids represent integrated atomic column intensities and peak locations/nearest-neighbors along [100]/[010] (X/Y) directions, respectively. The yellow/white and cyan/green markers represent Ba- and Cu/Zr-containing columns in REBCO and BZO, respectively. The 'compressed' images reveal that the I-0 type BZO has one unit cell less than REBCO along X but is fully coherent along Y direction. The I-I BZO has one unit cell less than REBCO in both directions. Both antiphase lines (where bonding shifts from Ba:Ba to Ba:Zr columns at REBCO:BZO interface) and dislocations (edge dislocation markers in) can be clearly distinguished, as well as the deformation field of the superimposed grids. The II-II type shown in (d) modulates in size between I-0/I-I and II-II type.

Shown in figure 2 are magnified plan (a)–(c) and cross section (d) views of I-0/I-I and II-II type BZO nanorods, respectively. For easy visualization, the plane view images have also been compressed along [100] and [010] directions. By examining the traces of the more intense Ba-containing columns along the horizontal direction of the REBCO/BZO interface in figure 2(a), the Ba–O columns in REBCO initially align with Ba–O in BZO, then show progressively higher misalignment until the bonding/alignment switches from Ba–O:Ba–O to Ba–O:Zr–O (REBCO:BZO) approximately midway, forming an 'antiphase line' which extends out of plane of the micrograph. Continuing further, a near-mirror image of the left-hand size of the interface appears, restoring Ba–O:Ba–O

alignment between REBCO and BZO. On the other hand, in the perpendicular [010] direction the interface is fully coherent, and 'elastic bending' of the lines joining the atom columns is readily observable. Clearly, the number of unit cells along the [100] direction in BZO is one less than the corresponding number of REBCO unit cells along the interface, while along [010], the number of unit cells is the same. With some ambiguity in the exact count due to the transition in intensity near the interfaces, the size of the nanorods is approximately 8–9 unit cells along the semi-coherent and coherent directions corresponding to the size of 3.3–3.7 nm.

Shown in figure 2(b) is the same I-0 type BZO nanorod but with a colormap and dots/grids superimposed

to the image. The dots/grids represent the atomic column locations and sublattices, where yellow/white represent Ba–Y(REBCO)/Ba(BZO) and green/cyan the Cu(REBCO)/Zr(BZO) containing columns. The superimposed colormap corresponds to the integrated intensity of atomic columns of the Ba-containing sublattices as a measure of average atomic number.

From the grids, one can readily identify the locations of the edge dislocations, which are marked in the image. The grids also clearly reveal the faceted growth of BZO where the nanorod consists of (100) and (110) type facets meeting approximately at the locations coincident with the edge dislocations. The strain states along [100] and [010] directions in BZO are clearly different, as evident from the grid deformation.

The signal intensity map separates the matrix and the precipitate based on average signal intensity. However, in the region near the interface, there exists a gradient in signal intensity, suggesting possible intermixing of ions along the interface or/and possible partial overlap of crystals in the thickness direction. Given the varying valence states between bonded columns (REBCO/BZO), intermixing to preserve charge neutrality and other crystal balance considerations is a viable scenario to explain the observed gradient. It should be noted that the top and bottom interfaces do show clear signs of crystal overlap, while the left and right 'elastic' interfaces do not exhibit such clear overlaps. Oxygen deficiency around BZO nanorods has been reported previously [82] and attributed to strain field at the BZO/REBCO interface. We note that oxygen non-stoichiometry at the interfaces can readily ensue due to local cation non-stoichiometry as well, particularly to satisfy local charge balance.

Shown in figure 2(c) is a micrograph of a I-I type BZO nanorod. Unlike I-0 type, one antiphase line and two edge dislocations can be observed along both (100) and (010) directions. Similar to the I-0 type, the I-I type nanorod also exhibits faceted growth and a gradient in signal intensity near the interface. The short (100)-type facets are bracketed by the dislocations and the long (110)-type facets form the rest of the interface. The bonding across the interfaces is Ba:Zr and Ba:Ba for (100) and (110)-type interfaces, respectively. The size of the observed I-I nanorods is larger compared to the I-0 type and is about 13 BZO unit cells.

The bottleshape modulation in nanorod diameter is illustrated in figure 2(d), in a cross-section view. In this case, nanorods grow as I-0 or I-I type followed by a gradual increase in diameter to the II-II type and then back to I-0 or I-I type, as shown. The maximum measured diameter in the bottleshape region over a large number of nanorods is approximately constant, within the uncertainty associated with determining the exact BZO/REBCO interface, and is in the range of 10.5–11 nm. This corresponds to approximately 25–27 BZO unit cells and is in good agreement with the expected strain minima for the II-II nanorod type, as discussed below.

We estimate the misfit strain associated with fitting a nanorod with N nanorod unit cells into a 'hole' in the matrix of M unit cells for the cases $N=M,\,N=M-1,\,N=M-2$ and N=M-P in general. This simple analysis is illustrated

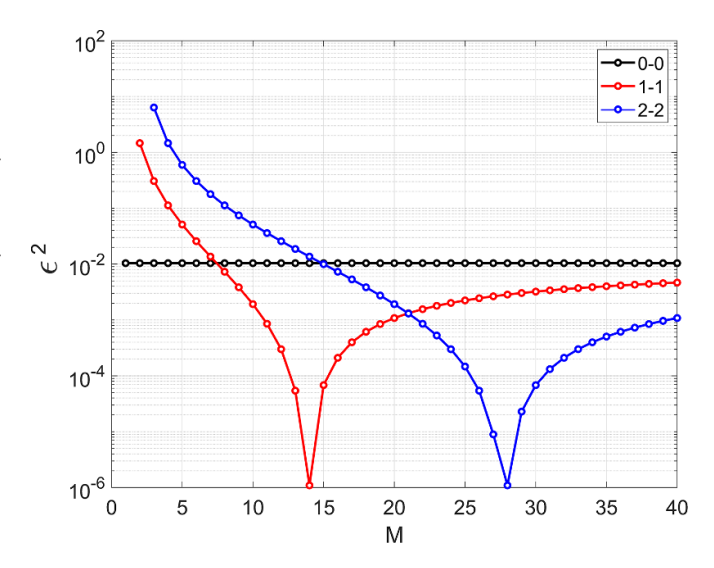


Figure 3. Sum of squares of in-plane principal strains for 0-0, I-I and II-II nanorods as a function of 'hole size' M—the number of REBCO unit cells. The corresponding nanorod sizes are N=M, M-1 and M-2 for 0-0, I-I and II-II types, respectively, where N is the number of nanorod unit cells. Sharp minima in strain energy are obtained at M=14 (N=13) for I-I type and M=28 (N=26) for II-II type. The corresponding I-I and II-II nanorod diameters at strain minima are ~ 5.4 and 10.8 nm, respectively.

in figure 3, where the square of misfit strain which represents a measure of misfit strain energy is plotted against the size of the hole in the REBCO matrix represented by the number of REBCO unit cells. As expected, for the 0-0 case, i.e. N = M, the misfit strain is constant and independent of the nanorod size. In this case, there is no preference for a single isolated nanorod to assume any particular diameter, and the diameter with minimum energy may be obtained if, e.g. volume fraction of BZO is constrained and the strain interaction between nanorods is taken into account, or if an interface energy proportional to interface area is assumed, as has been done in, e.g. [16, 40, 75]. However, for the I-I case (N = M - 1), the strain energy has a sharp minimum at $M \approx 14$ (N = 13) which is orders of magnitude lower than that for the 0-0 case. Similarly, at M \approx 28 (N = 26), another sharp minimum occurs for the II-II case. The nanorods are able to assume their discrete energy minima sizes even in the case of very low density of nanorods—towards the limit of a single isolated nanorod in a continuous REBCO matrix.

If a_M and a_N are lattice parameters of the matrix and nanorod, respectively, and $k = a_M/a_N$, then mismatch strain can be represented as

$$\epsilon = \frac{M}{M - P}k - 1\tag{1}$$

and the minimum of the strain energy ε^2 measure can be found at the rounded value of

$$M = \left(\frac{1}{1-k}\right)P. (2)$$

The unit cell parameters depend on a number of factors including REBCO non-stoichiometry and Zr content [48, 63].

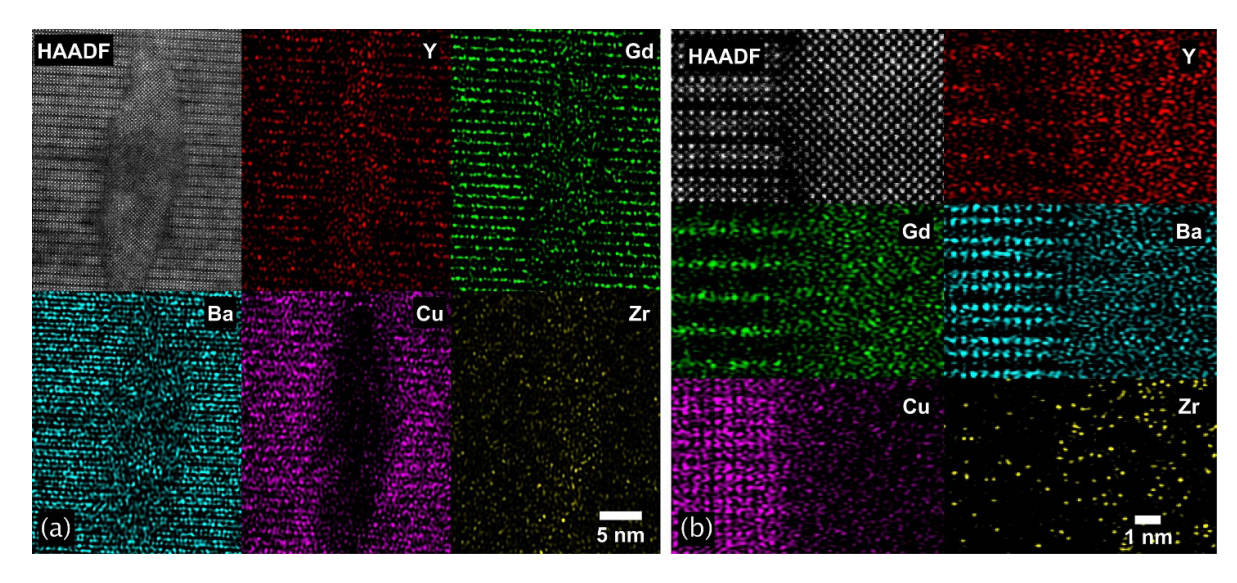


Figure 4. Cross-section HAADF image and EDS elemental maps of the bottleshape region of two BZO nanorods. While the Cu signal drops to noise level inside BZO, indicating no significant overlap between BZO and REBCO in this TEM sample, Y and Gd signal, surprisingly, reveals presence of both elements in the BZO nanorods, suggesting a solid solution of Y and Gd in the nominal BZO nanorods.

For the samples evaluated in this study, we adopt the unit cell values of tetragonal (as-grown) REBCO and BZO as a = 3.86and 4.16 Å, respectively, based on our estimates from 2D-XRD. With these numbers, we arrive at N \approx 14 and 28 for P = 1 and 2, respectively, which corresponds to M = 13 and 26, respectively. These M values provide an estimate for equilibrium nanorod diameters for the I-I and II-II types of 5.4 and 10.8 nm, respectively, which is in very good agreement with our TEM observations. It should be noted that the minimum strain energy calculated for the I-O nanorod does not predict the observed size of \sim 3.8 nm but instead has a minimum at the same M and N values as for the I-I nanorod. The strain distribution for the I-0 case is anisotropic in the x and y (or [100]/[010]) directions, as evident from figure 2, which would require a more detailed model. Nevertheless, this simple misfit strain minimization outlined above capture the nature of the problem and results are in good agreement with the experimentally observed I-I and II-II nanorod sizes.

We note that the interfaces contain excess energy introduced by the misfit dislocations, change in nearest neighbor environments at the antiphase line and other considerations such as the lack of Cu–O column peaks in the REBCO phase near the antiphase line, as well as a degree of overlap between BZO and REBCO in this region. Local electroneutrality and related considerations are likely to affect this region and need to be taken into account, and experimental evidence does indicate local change in oxygen content near the interfaces [82].

Next, we point out that in-plane mismatch accommodation is only one aspect of total strain energy. While in-plane mismatch accommodation is the focus of this study, the elastic mismatch along the REBCO c-axis is an equally important aspect of film growth and nanorod self-assembly. We have reported earlier that the same metric, (Ba + Zr)/Cu, has a considerable effect on c-axis lattice mismatch between BZO and REBCO [48, 61, 63]. Multiple studies have reported presence

of dense arrays of REBCO 124/248 type, 223 and other stacking faults [54, 83–91], and we have regularly observed the same features, as can also be seen in figure 2(d). One can readily envision a mismatch strain accommodation between c-axis of BZO and REBCO by inserting extra Cu–O planes to form 124-type defect at regular intervals in REBCO matrix to minimize mismatch between REBCO and BZO along the c-axis.

3.2. Elemental distribution

Shown in figure 4 are cross-section EDS maps of two size-modulated, bottleshape BZO nanorods taken at two magnifications. In the lower magnification figure 4(a), the HAADF-STEM image and Cu elemental map show no overlap of BZO with the host REBCO matrix for this thin TEM sample in this projection, as evidenced by the drop in Cu signal to the noise level in the BZO section. The Ba map shows presence of Ba in both REBCO and BZO, as expected. On the other hand, remarkably, Gd and Y levels do not drop to noise level in the BZO nanorod, as would be expected if BZO is pure phase. The Y signal in particular appears stronger in BZO than in the host REBCO suggesting dissolution of RE in BZO nanorods. A higher magnification image and EDS maps of REBCO/BZO interface from another bottleshape nanorod are presented in figure 4(b). The results are consistent with the maps shown in figure 4(a): Cu drops to noise level in BZO, Zr signal is weak, and again Y and Gd levels are significant in

EDS maps were also obtained in plan-view, as shown in figure 5 for (a) high and (b) low magnifications. The Y, Ba and Zr atomic columns are resolved in the high magnification maps. The overlap Ba + Y and Ba + Zr maps show distinct atomic columns for Ba and Y + Zr, where Y and Zr sites coincide. These results strongly suggest Y solid solution on the Zr site. The Gd maps are less defined; however, the significant

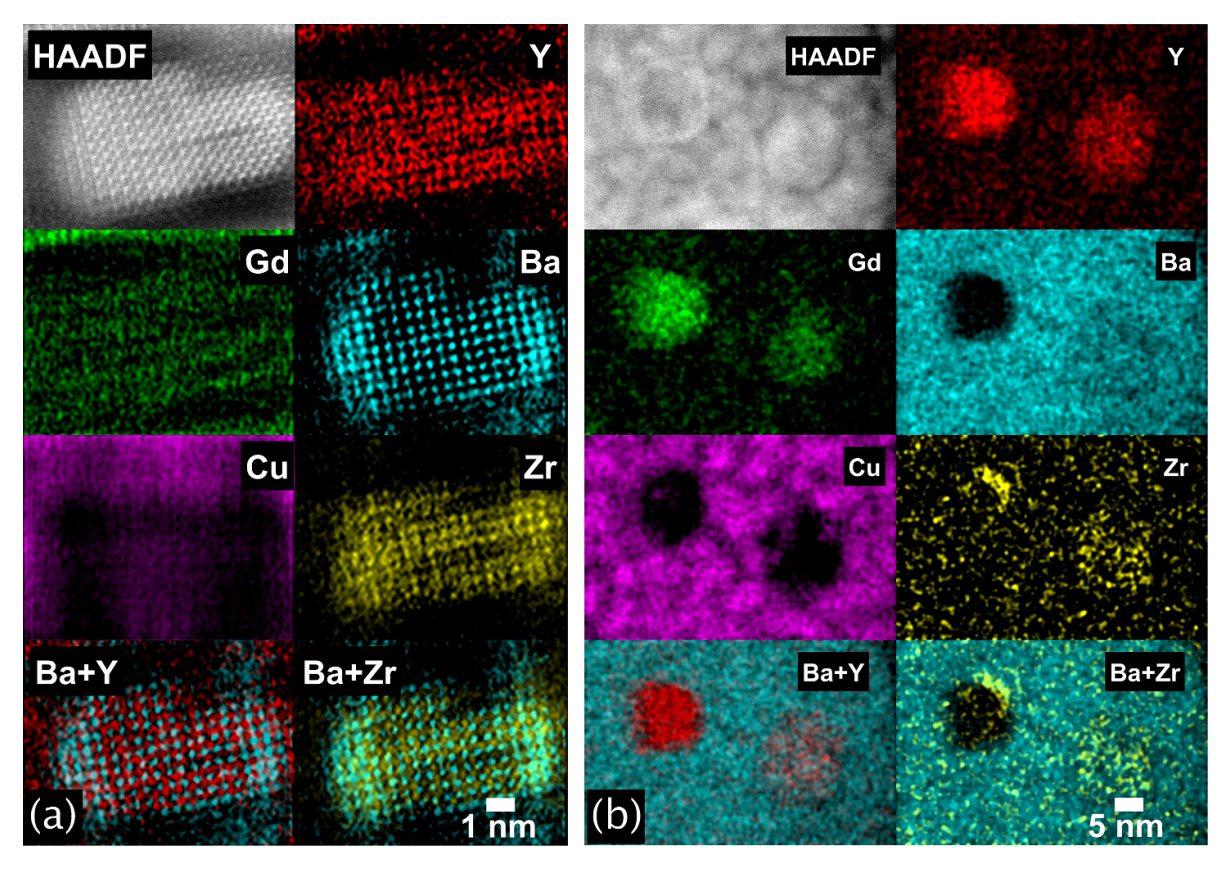


Figure 5. (a) Plan-view HAADF STEM image and EDS analysis of a BZO nanorod. The unexpected features are strong presence of Y in BZO, atomically resolved to match the nominal Zr sites in BZO. The Gd map also suggests dissolution of Gd in BZO. (b) Lower magnification analysis of REO (left) and BZO (right) precipitates, as confirmed by Fourier analysis. The expected features are absence of Cu in both particles and presence of Ba in BZO but not in REO. However, the unexpected features are strong presence of both Y and Gd in BZO, suggesting dissolution of RE in BZO. The Zr map reveals segregation of Zr in REBCO over a part of the interface with REO.

(above noise) level of Gd in the maps suggests that Gd is also present in BZO matrix.

Figure 5(b) captures two precipitates at lower magnification, REO to the left and BZO to the right, as confirmed by Fourier transform analysis of the respective sections of the image. As expected, Ba is present in BZO but absent in REO. Cu is absent in both precipitates, again as expected. However, Y and Gd maps show their strong presences in both REO and BZO with both signals being above the noise level (they are expected to be in REO). These observations undoubtedly confirm the presence of both Y and Gd in BZO. Surprisingly, we also observed an unexpected finding of segregation of Zr near the REO particle.

We conclude that RE substitutes for Zr in BZO, Y is present on Zr sites in BZO, and that Zr is not entirely contained within BZO, as evidenced by Zr segregation around REO. These results suggest potentially strong departures of both BZO and REO volume/unit cell fractions relative to the expectations based on nominal composition (in this case 15 mol. % Zr and 30% mol.% excess RE).

3.3. Volumetric densities of BZO and REO

The presented results on RE dissolution in BZO have significant consequences on stoichiometry, composition and volume

fraction of BZO and REO. Here, we evaluate the magnitude of these effects from lower resolution micrographs obtained by conventional TEM in order to obtain statistically meaningful results over larger examined areas.

We have reported earlier a strong effect of the starting MOCVD precursor composition on in-field performance and microstructure characteristics of the resulting Zr-doped REBCO films [13, 15, 48, 61, 63], in particular by varying Ba content. One striking earlier observation was that the REB-CO/BZO system can tolerate large departures from nominal Ba content and still form single phase REBCO, BZO and REO only [48, 63].

The dissolution of RE into BZO suggests a possible explanation for the observed behavior. In the simplest scenario, if we assume that all added Zr must end in BZO, then the additional dissolution of RE onto Zr sites in BZO implies larger volume fraction of BZO than the expected nominal value. In addition, if all Zr is included in BZO and additional RE is dissolved in BZO, this scenario implies the necessity of having available excess Ba beyond that needed to form REBCO and the nominal BZO, one ion per each RE ion included in BZO:

BaZrO₃ + xBa + xRE =
$$(1+x)$$
Ba $\left(Zr_{\frac{1}{1+x}}RE_{\frac{x}{1+x}}\right)$ O₃. (3)

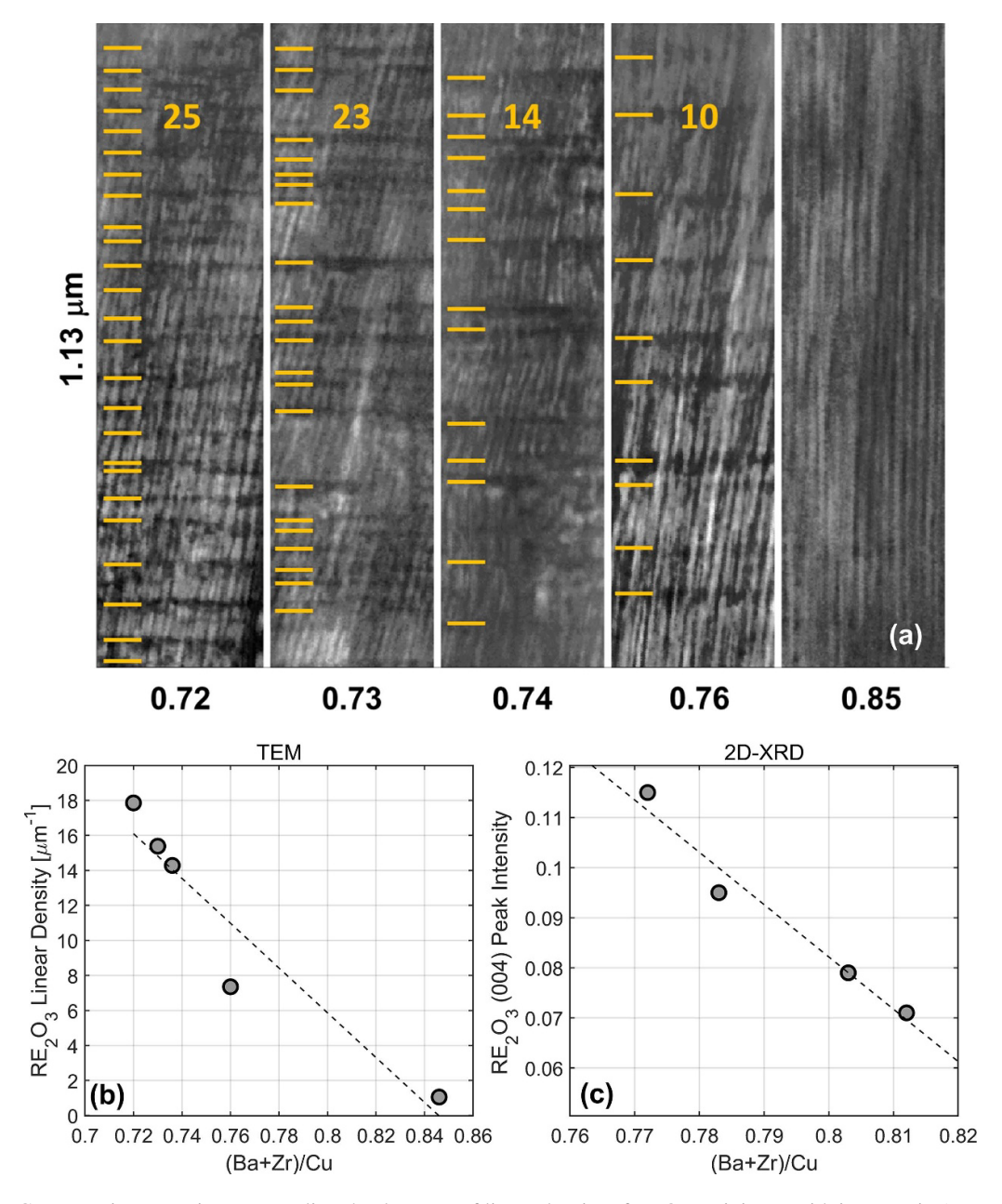


Figure 6. (a)—Cross-section TEM image revealing the decrease of linear density of REO precipitates with increase in (Ba + Zr)/Cu content, indicated at the bottom of micrographs. The REO rows are marked with orange lines and their count indicated in orange font. Also shown are estimates of (b)—REO linear density from TEM micrographs and (c)—REO content from (004) peak intensity obtained from 2D-XRD (from a different set of samples) as a function of (Ba + Zr)/Cu. Both methods confirm strong reduction in REO content with increasing (Ba + Zr)/Cu.

The nominal stoichiometric Ba content supplies 2 Ba atoms per REBCO unit cell and y Ba atoms for y Zr atoms added, i.e. 2.15 for 15 mol.% Zr addition, or (Ba + Zr)/Cu = 0.767. Additional Ba is then expected to increase BZO and reduce REO content. To verify this assumption, we analyze the BZO and REO content of five samples with 15 mol.% Zr addition and varying Ba content using conventional TEM.

3.4. REO precipitates

Shown in figure 6(a) is a series of five cross-section micrographs corresponding to samples with increasing (Ba + Zr)/Cu

ratio from under-compensated (0.72) to over-compensated (0.85). The REO precipitates regularly form as rows of nearly-'spherical' (low aspect ratio) precipitates in well separated layers parallel to REBCO a-b planes, as shown in the figure and reported in other studies such as [5, 15, 41, 92, 93]. As can be seen, the linear density of these REO rows along the c-axis decreases with increasing Ba content, resulting in almost complete absence of REO in the sample with (Ba + Zr)/Cu = 0.85. The corresponding plot of REO density (in 1 μ m⁻¹ units) vs (Ba + Zr)/Cu content is shown in figure 6(b). The linear density of 'rows' of REO precipitates decreases near-linearly with increase in (Ba + Zr)/Cu content. We confirmed

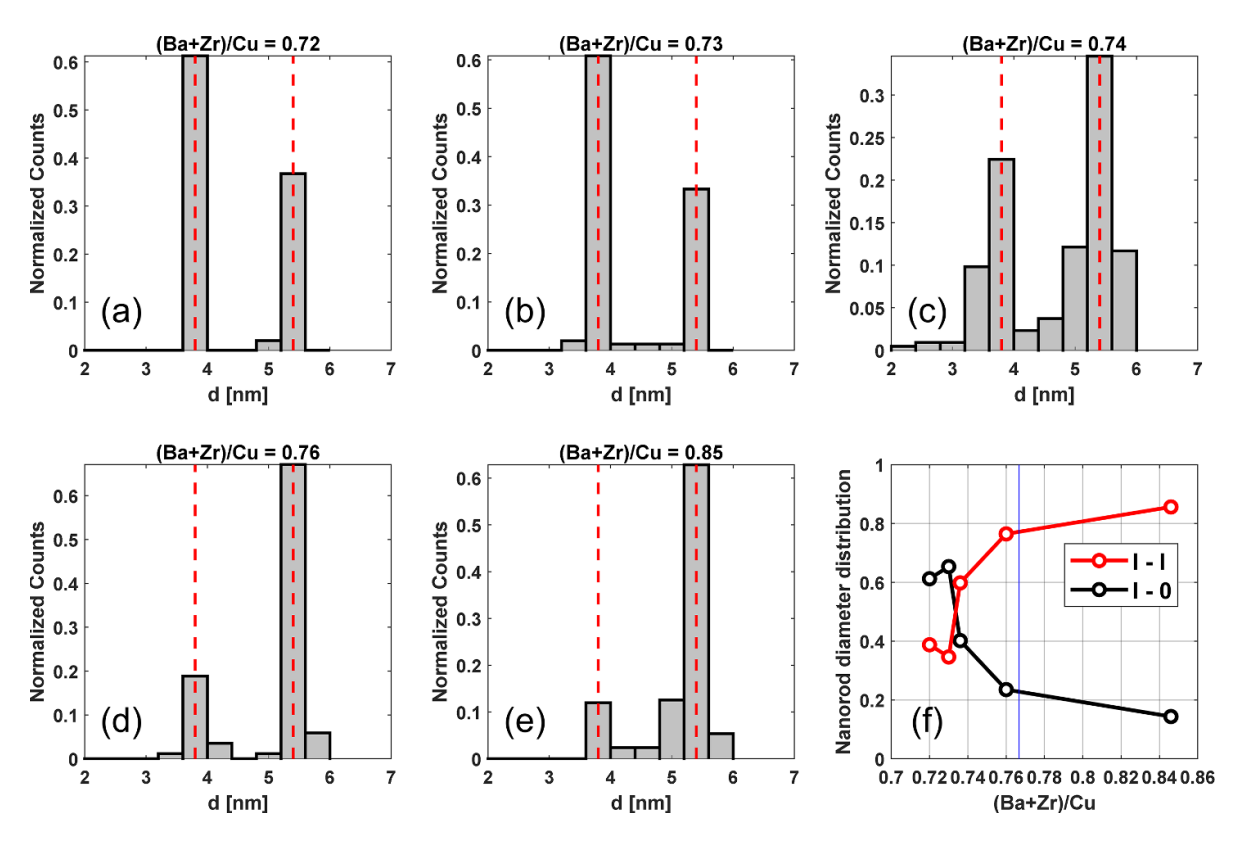


Figure 7. (a)—(e) Nanorod size distribution as a function of (Ba + Zr)/Cu content, determined from TEM micrographs, revealing a bimodal distribution of two predominant sizes that match I-0 and I-I type nanorods. (f)—Relative amounts of I-0 and I-I type nanorods as a function of (Ba + Zr)/Cu.

these TEM findings with 2D-XRD measurements on a different set of samples by evaluating the REO (004) peak intensity as a function of (Ba + Zr)/Cu, as shown in figure 6(c).

3.5. BZO nanorods

The nanorod size distribution as a function of (Ba + Zr)/Cu is given in figures 7(a)–(e), as determined from conventional TEM images, including a total of 668 nanorods. As can be seen, the size distribution is bimodal, i.e. in all samples, two nanorod sizes are predominant: 3.8 and 5.4 nm. These values agree with the findings from high resolution Cs-STEM micrographs that have identified only I-0, I-I and II-II nanorod types.

Shown in figure 7(f) are summarized results on the relative distribution of I-0 vs I-I type nanorods, as a function of (Ba + Zr)/Cu. For undercompensated Ba samples, (Ba + Zr)/Cu < 0.767, the nanorod size sharply decreases with decrease in (Ba + Zr)/Cu content towards predominantly I-0 type. For overcompensated Ba samples, the nanorod size is predominantly I-I type. The size distribution of nanorods is likely affected by other parameters such as growth rate [6, 21, 38, 94], which is primarily determined by the incident flux of atoms on the growing film. This would correspond to target-to-sample atom flux in PLD and concentration and flow rate and molarity of precursor in the case of MOCVD. In our previously reported study, we show that it is possible to grow films with extremely high density and very uniform

size distribution that most closely match in size to the I-0 type [13]. While the (Ba + Zr)/Cu content was comparable to the sample with the highest (Ba + Zr)/Cu value presented in this study, we do note that the deposition rate for the sample with high density of nanorods reported in previous work [13] was double compared to the samples analyzed here. The deposition rate was held constant and the effect of deposition rate was not considered in the present study. However, these considerations do indicate possible effect of growth kinetics on nanorod size distribution, implying that the films are not at true thermodynamic equilibrium, and the need to address this aspect in a separate study.

Next, we analyze the effect of (Ba + Zr)/Cu on nanorod spacing with the results summarized in figure 8, where the nanorod areal density as well as the corresponding matching field as a function of (Ba + Zr)/Cu are presented. The results of a separate analysis performed on a different set of samples are plotted together for comparison. The data reveal a striking effect of Ba content on the resulting nanorod density. For the nominal 15% Zr addition, nanorod density varies from 1000 to over 4000 μ m⁻² and matching field from 2 to over 8 T (for the sample reported in [13], the matching field was 17 T, despite only 11% Zr addition). It becomes clear that the amount of Zr addition itself is not an indicator of nanorod density and thus pinning performance. Ba non-stoichiometry, on the other hand, has a strong role in the resulting nanorod landscape characteristics. If the potential strong effect of deposition rate/kinetics is also considered [6, 38, 94], it becomes

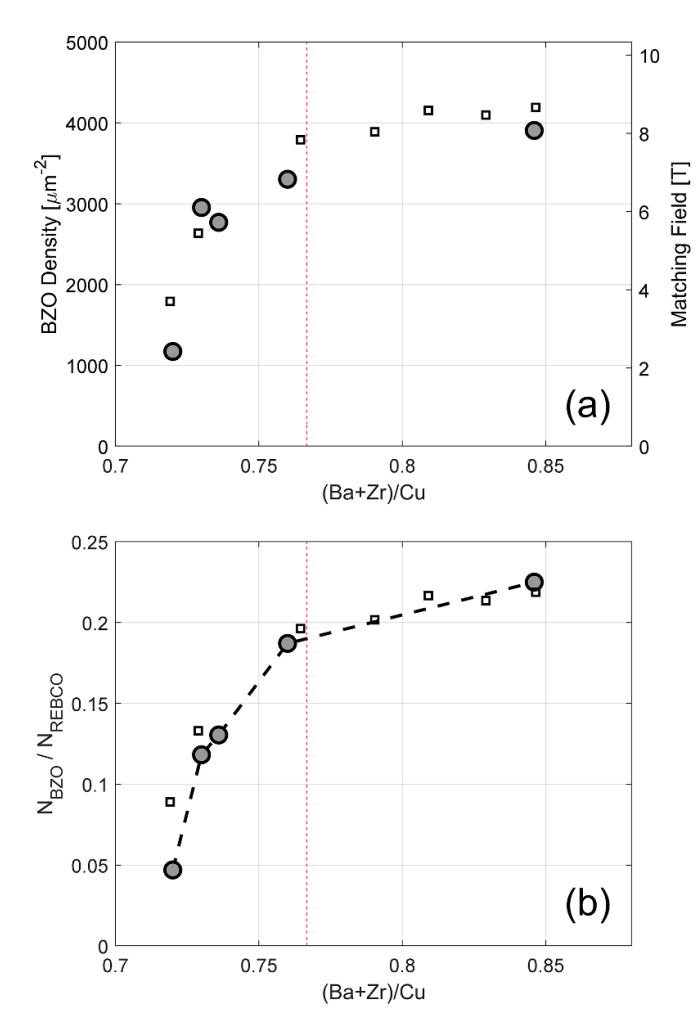


Figure 8. Nanorod characteristics as a function of (Ba + Zr)/Cu. (a)—BZO areal density and the corresponding matching field as determined from plan-view TEM micrographs. (b)—calculated unit cell fraction of BZO relative to REBCO, as determined from nanorod areal density and size distribution. The large circle markers represent the same samples analyzed in figure 6. All samples contained nominal 15% Zr addition, the nominal fully compensated composition (Ba + Zr)/Cu = 0.767 is indicated with the red dashed line. The results indicate large variation in BZO content as a function of (Ba + Zr)/Cu.

evident that the nanorod landscape could be tuned over a wide range of size and spacing distributions for the same nominal Zr content.

The BZO nanorod unit cell fraction relative to REBCO was also estimated based on nanorod size distribution and areas determined from Voronoi segmentation based on nanorod center locations. The results are presented in figure 8(b). The results are again surprising in that the nominal addition of 15% Zr results in samples with BZO unit cell fractions ranging from 5% to -23% depending on Ba nonstoichiometry, which is included in the (Ba + Zr)/Cu variable. If dissolution of RE elements into nominal BZO is included into consideration, as discussed earlier, the increase in unit cell fraction of nanorods beyond the nominal 15% Zr addition is expected. However, the mechanism behind the drastic decrease in BZO fraction to near 5% is still less clear. The Zr segregation

around REO precipitates is one possible route to accommodate the excess 10% Zr. Other possible mechanisms, such as dissolution of Zr in REO, as reported in [95, 96], should also be considered. A further in-depth study on under-compensated Ba samples is needed to provide more evidence related to this strong decrease in nanorod content.

The dissolution of RE into BZO is likely to affect properties other than the mere changes in volume fractions of BZO and REO precipitates. Doped BaZrO₃ perovskites have been extensively studied as a prospective electrolyte for hydrogen separation membranes, solid oxide fuel cells and gas sensors [97–106], by substituting a fraction of the B^{4+} cations with C^{3+} (Y, Gd, Al, Sc, Sm, Nd, La, etc) to form $AB_{1-x}C_xO_3$, resulting in creation of oxygen vacancies to maintain charge equilibrium, which in turn increases either oxygen or proton permeability. In the present case, Zr⁺⁴ is substituted by RE³⁺. In addition to permeability studies, this comprehensive literature also reports on the effect of various dopants and their amounts on the elastic constants, lattice parameters and other properties [98, 99]. The Young's and Bulk moduli have been reported to decrease by 20% and lattice parameter to increase from 4.19 to 4.23 Å with increase in Y doping from x = 0–0.2. These effects will contribute lattice mismatch and elastic energy in the BZO/REBCO system. In our previously reported study on 25% Zr addition to REBCO, the BZO lattice parameter was found to decrease as a function of (Ba + Zr)/Cu content going from 4.24 to 4.08 Å with increase in (Ba + Zr)/Cu (from 0.55 to 0.83), while simultaneously resulting in increase in REBCO c-axis lattice parameter and, thereby, reducing c-axis lattice mismatch from 8% to 3% [48]. In the present study, the increase from 18% to 23% constitutes approximately 28% increase in nanorod unit cell content, which is comparable with the frequently used doping of RE into BZO of 20% [99, 104] and the reported phase diagram solubility of RE of 30% [106].

4. Conclusions

Atomic resolution Cs-TEM and compositional EDS analysis of BZO nanorods in REBCO matrix show several new and critical observations about the BZO/REBCO system. In-plane mismatch between BZO nanorods and REBCO matrix is minimized by growth of BZO nanorods with integer number of unit cells smaller than the corresponding hole in the REBCO matrix. Three types of nanorods are identified, referred as I-0, I-I and II-II type with roman numerals denoting the difference in the number of unit cells of REBCO and BZO along two perpendicular [100]/[010] crystallographic directions. Each missing unit cell in BZO results in formation of two interface dislocations. None of the nanorods examined were purely coherent or elastically accommodated. The misfit strain has strong minima, orders of magnitude lower compared to coherent interfaces, at 14/13 and 28/26 REBCO/BZO unit cells for the I-I and II-II types, corresponding to nanorod sizes of 5.4 and 10.8 nm, respectively. The I-0 type nanorod consists of 8 and 9 unit cells along the perpendicular semicoherent (I) and coherent (0) directions, with sizes of 3.3–3.7 nm, respectively. Statistical measures of nanorod size over large number of nanorods

imaged by conventional TEM confirm the findings, revealing bimodal size distribution at diameters centered at 3.8 and 5.4 nm, consistent with I-0 and I-I type nanorods.

The nominal BZO nanorods have been found to contain significant amount of RE elements on the Zr–O sublattice, forming a $Ba^{2+}(Zr^{4+}{}_{1-x}RE^{3+}{}_x)O_{3-\delta}$ perovskite. This provides a mechanism of absorbing excess Ba relative to the nominal composition. This effect of Ba non-stoichiometry on the amount of BZO and REO precipitates has been determined. Increase of excess Ba results in monotonic increase in the amount of BZO and reduction in REO content. For the same nominal Zr and RE additions of 15 unit cell% BZO and 15% RE₂O₃, the amount of BZO and REO precipitates varies over a wide range as a function of Ba excess or deficiency. Despite the constant nominal 15% Zr addition, the BZO unit cell content varies from 5% to 23% while REO linear density simultaneously decreases from 18 to >1 μ m⁻¹ with increase in Ba content from Ba-deficient to Ba-rich stoichiometry.

The presented results reveal in-plane mismatch accommodation mechanisms and demonstrate the far reaching consequences of composition of the REBCO/BZO system. The findings provide insight into potential paths for engineering the system towards optimum performance or, alternatively, for analyzing or choosing the optimum dopant for BMO nanorods.

Data availability statement

All data that support the findings of this study are included within the article (and any supplementary files).

Acknowledgments

This work was partly funded by the U.S. Department of Energy Award DE-SC0016220. We acknowledge University of Houston Division of Research High Priority Area Research Large Equipment Grant I0503304 for establishing a state-of-the-art 2D-XRD facility used in this study.

This work is partially supported by National Science Foundation through UMN MRSEC. under Awards DMR-1420013 and DMR-2011401. This work utilized the UMN Characterization Facility, supported in part by the NSF through the UMN MRSEC program.

The authors wish to express their gratitude to Thermo Fisher Scientific and the NanoPort-Portland team for their invaluable support with HRTEM (Dr D Gostovic, Dr L Pullan, Dr L Brock and Dr L Casalena).

ORCID iDs

Goran Majkic https://orcid.org/0000-0003-0168-0856 Francisco C Robles Hernandez https://orcid.org/0000-0001-5587-0802

Eduard Galstyan https://orcid.org/0000-0003-1486-6449 Venkat Selvamanickam https://orcid.org/0000-0001-6618-9406

References

- [1] Majkic G, Pratap R, Paidpilli M, Galstyan E, Kochat M, Goel C, Kar S, Jaroszynski J, Abraimov D and Selvamanickam V 2020 Supercond. Sci. Technol. 33 07LT03
- [2] Namburi D K 2020 Supercond. Sci. Technol. 33 090502
- [3] Majkic G, Pratap R, Xu A X, Galstyan E, Higley H C, Prestemon S O, Wang X R, Abraimov D, Jaroszynski J and Selvamanickam V 2018 Supercond. Sci. Technol. 31 10LT01
- [4] Obradors X 2018 Supercond. Sci. Technol. 31 3
- [5] Majkic G, Pratap R, Xu A X, Galstyan E and Selvamanickam V 2018 Sci. Rep. 8 6982
- [6] Miura S, Yoshida Y, Ichino Y, Xu Q, Matsumoto K, Ichinose A and Awaji S 2016 APL Mater. 4 016102
- [7] Matsumoto K and Mele P 2010 Supercond. Sci. Technol. 23 014001
- [8] Macmanus-Driscoll J L, Foltyn S R, Jia Q X, Wang H, Serquis A, Civale L, Maiorov B, Hawley M E, Maley M P and Peterson D E 2004 Nat. Mater. 3 439–43
- [9] Selvamanickam V, Gharahcheshmeh M H, Xu A, Zhang Y and Galstyan E 2015 Supercond. Sci. Technol. 28 5
- [10] Tobita H, Notoh K, Higashikawa K, Inoue M, Kiss T, Kato T, Hirayama T, Yoshizumi M, Izumi T and Shiohara Y 2012 Supercond. Sci. Technol. 25 062002
- [11] Goyal A et al 2005 Supercond. Sci. Technol. 18 1533-8
- [12] Yamada Y et al 2005 Appl. Phys. Lett. 87 132502
- [13] Majkic G, Pratap R, Galstyan E, Xu A X, Zhang Y and Selvamanickam V 2017 IEEE Trans. Appl. Supercond. 27 6602605
- [14] Peurla M, Paturi P, Stepanov Y P, Huhtinen H, Tse Y Y, Bódi A C, Raittila J and Laiho R 2006 Supercond. Sci. Technol. 19 767–71
- [15] Galstyan E, Pratap R, Majkic G, Kochat M, Mohan V and Selvamanickam V 2019 IEEE Trans. Appl. Supercond. 29 8001206
- [16] Wu J Z, Shi J J, Baca F J, Emergo R, Wilt J and Haugan T J 2015 Supercond. Sci. Technol. 28 125009
- [17] Wu J et al 2019 IEEE Trans. Appl. Supercond. 29 8001105
- [18] Gautam B et al 2018 Appl. Phys. Lett. 113 212602
- [19] Stafford B H, Sieger M, Ottolinger R, Meledin A, Strickland N M, Wimbush S C, Van Tendeloo G, Huhne R and Schultz L 2017 Supercond. Sci. Technol. 30 055002
- [20] Pahlke P et al 2016 IEEE Trans. Appl. Supercond. 26 6603104
- [21] Ichino Y, Tsuruta A, Miura S, Yoshida Y, Yoshizumi M and Izumi T 2015 IEEE Trans. Appl. Supercond. 25 6604506
- [22] Kotaki T, Uraguchi Y, Makihara T, Suenaga M, Sueyoshi T, Fujiyoshi T, Mitugi F and Ikegami T 2015 *Physica C* 518 63–68
- [23] Yoshida T, Ibi A, Takahashi T, Yoshizumi M, Izumi T and Shiohara Y 2014 Physica C 504 42–46
- [24] Tran D H, Putri W B K, Kang B, Lee N H and Kang W N 2014 J. Appl. Phys. 115 163901
- [25] Sieger M et al 2017 IEEE Trans. Appl. Supercond. 27 6601407
- [26] Opherden L et al 2016 Sci. Rep. 6 21188
- [27] Feldmann D M, Holesinger T G, Maiorov B, Foltyn S R, Coulter J Y and Apodaca I 2010 Supercond. Sci. Technol. 23
- [28] Xu Y, Suo H L, Grivel J-C, Liu M, Zhang X L, Zhou Y Q, Liu J H and Zhang Z L 2020 Cryst. Growth Des. 20 3449–55
- [29] Kai H, Horii S, Ichinose A, Kita R, Matsumoto K, Yoshida Y, Fujiyoshi T, Teranishi R, Mori N and Mukaida M 2010 Supercond. Sci. Technol. 23 025017

- [30] Horii S et al 2007 Supercond. Sci. Technol. 20 1115–9
- [31] Miura M, Maiorov B, Willis J O, Kato T, Sato M, Izumi T, Shiohara Y and Civale L 2013 Supercond. Sci. Technol. 26 035008
- [32] Ding F Z, Gu H W, Zhang T, Wang H Y, Qu F, Qiu Q Q, Dai S T, Peng X Y and Cao J-L 2014 *Appl. Surf. Sci.* 314 622–7
- [33] Ye S, Suo H L, Wu Z P, Liu M, Xu Y, Ma L and Zhou M L 2011 *Physica* C **471** 265–9
- [34] Santiso J, Figueras A, Schamm S, Grigis C, Dorignac D and Sevely J 1994 *Physica* C **235** 619–20
- [35] Rivasto E, Khan M Z, Malmivirta M, Rijckaert H, Aye M M, Hynninen T, Huhtinen H, Van Driessche I and Paturi P 2020 Sci. Rep. 10 3169
- [36] Horide T, Torigoe K, Kita R, Nakamura R, Ishimaru M, Awaji S and Matsumoto K 2019 J. Japan Inst. Met. Mater. 83 320–6
- [37] Horide T, Nagao S, Izutsu R, Ishimaru M, Kita R and Matsumoto K 2018 Supercond. Sci. Technol. 31 065012
- [38] Ichino Y and Yoshida Y 2017 IEEE Trans. Appl. Supercond. 27 7500304
- [39] Tsuchiya Y, Miura S, Xu Q Y, Ichino Y, Yoshida Y, Awaji S and Watanabe K 2017 IEEE Trans. Appl. Supercond. 27 8000805
- [40] Shi J J and Wu J Z 2015 J. Appl. Phys. 118 164301
- [41] Xu A X et al 2015 IEEE Trans. Appl. Supercond. 25 5
- [42] Xu A, Delgado L, Gharahcheshmeh M H, Khatri N, Liu Y and Selvamanickam V 2015 Supercond. Sci. Technol. 28 6
- [43] Shi J J and Wu J Z 2012 Phil. Mag. 92 2911-22
- [44] Wang X, Baca F J, Emergo R L S, Wu J Z, Haugan T J and Barnes P N 2010 J. Appl. Phys. 108 14682
- [45] Ichinose A, Naoe K, Horide T, Matsumoto K, Kita R, Mukaida M, Yoshida Y and Horii S 2007 Supercond. Sci. Technol. 20 1144–50
- [46] Iijima Y *et al* 2017 *IEEE Trans. Appl. Supercond.* **27** 6602804
- [47] Miura S, Yoshida Y, Ichino Y, Tsuruta A, Matsumoto K, Ichinose A and Awaji S 2015 IEEE Trans. Appl. Supercond. 25 6604904
- [48] Gharahcheshmeh M H, Majkic G, Galstyan E, Xu A, Zhang Y, Li X-F and Selvamanickam V 2018 *Physica* C 553 26–32
- [49] Malmivirta M, Rijckaert H, Paasonen V, Huhtinen H, Hynninen T, Jha R, Awana V S, Van Driessche I and Paturi P 2017 Sci. Rep. 7
- [50] Selvamanickam V, Gharahcheshmeh M H, Xu A, Galstyan E, Delgado L and Cantoni C 2015 Appl. Phys. Lett. 106 5
- [51] Malmivirta M, Yao L D, Huhtinen H, Palonen H, Van Dijken S and Paturi P 2014 Thin Solid Films 562 554–60
- [52] Lei C H, Galstyan E, Chen Y M, Shi T, Liu Y H, Khatri N, Liu J F, Xiong X M, Majkic G and Selvamanickam V 2013 IEEE Trans. Appl. Supercond. 23 4
- [53] Majkic G, Yao Y, Liu J G, Liu Y H, Khatri N D, Shi T, Chen Y M, Galstyan E, Lei C H and Selvamanickam V 2013 IEEE Trans. Appl. Supercond. 23 5
- [54] Wee S H, Zuev Y L, Cantoni C and Goyal A 2013 Sci. Rep. 3 2310
- [55] Selvamanickam V, Yao Y, Chen Y, Shi T, Liu Y, Khatri N D, Liu J, Lei C, Galstyan E and Majkic G 2012 Supercond. Sci. Technol. 25 7
- [56] Augieri A et al 2010 J. Appl. Phys. 108 5
- [57] Feldmann D M, Holesinger T G, Maiorov B, Zhou H, Foltyn S R, Coulter J Y and Apodoca I 2010 Supercond. Sci. Technol. 23 115016
- [58] Zhou H, Maiorov B, Baily S A, Dowden P C, Kennison J A, Stan L, Holesinger T G, Jia Q X, Foltyn S R and Civale L 2009 Supercond. Sci. Technol. 22 085013

- [59] Sieger M, Hanisch J, Iida K, Gaitzsch U, Rodig C, Schultz L, Holzapfel B and Huhne R 2014 Pulsed laser deposition of thick BaHfO3-doped YBa2Cu3O7-delta films on highly alloyed textured Ni-W tapes 11th European Conf. on Applied Superconductivity ed S Farinon et al
- [60] Majkic G 2020 Progress in thick film 2G-HTS development Superconductivity ed P Mele et al (Berlin: Springer) pp 73–131
- [61] Gharahcheshmeh M H, Galstyan E, Kukunuru J, Katta R, Majkic G, Li X-F and Selvamanickam V 2017 IEEE Trans. Appl. Supercond. 27 6602905
- [62] Majkic G, Pratap R, Galstyan E and Selvamanickam V 2019 IEEE Trans. Appl. Supercond. 29 5
- [63] Gharahcheshmeh M H, Galstyan E, Xu A, Kukunuru J, Katta R, Zhang Y, Majkic G, Li X-F and Selvamanickam V 2017 Supercond. Sci. Technol. 30 015016
- [64] Xu A et al 2017 Sci. Rep. 7 6853
- [65] Xu A X, Zhang Y, Gharahcheshmeh M H, Delgado L, Khatri N, Liu Y H, Galstyan E and Selvamanickam V 2017 IEEE Trans. Appl. Supercond. 27 4201005
- [66] Selvamanickam V, Gharahcheshmeh M H, Xu A, Zhang Y and Galstyan E 2015 Supercond. Sci. Technol. 28 5
- [67] Xu A, Delgado L, Khatri N, Liu Y, Selvamanickam V, Abraimov D, Jaroszynski J, Kametani F and Larbalestier D C 2014 APL Mater. 2 8
- [68] Selvamanickam V et al 2013 Supercond. Sci. Technol. 26 9
- [69] Selvamanickam V, Chen Y, Zhang Y, Guevara A, Shi T, Yao Y, Majkic G, Lei C, Galtsyan E and Miller D J 2012 Supercond. Sci. Technol. 25 6
- [70] Aye M M, Khan M Z, Rivasto E, Tikkanen J, Huhtinen H and Paturi P 2019 *IEEE Trans. Appl. Supercond.* 29 8000805
- [71] Matsumoto K, Horide T, Jha A K, Mele P, Yoshida Y and Awaji S 2015 IEEE Trans. Appl. Supercond. 25 8001106
- [72] Strickland N M, Long N J, Talantsev É F, Hoefakker P, Xia J, Rupich M W, Kodenkandath T, Zhang W, Li X and Huang Y 2008 Physica C 468 183–9
- [73] Galstyan E, Pratap R, Majkic G, Kochat M, Abraimov D, Jaroszynski J and Selvamanickam V 2020 Supercond. Sci. Technol. 33 074007
- [74] Molodyk A et al 2021 Sci. Rep. 11 2084
- [75] Wu J Z, Shi J J, Baca J F, Emergo R, Haugan T J, Maiorov B and Holesinger T 2014 Supercond. Sci. Technol. 27 044010
- [76] Wu J and Shi J 2017 Supercond. Sci. Technol. 30 103002
- [77] Arendt P N and Foltyn S R 2011 MRS Bull. 29 543-50
- [78] Xiong X, Kim S, Zdun K, Sambandam S, Rar A, Lenseth K P and Selvamanickam V 2009 IEEE Trans. Appl. Supercond. 19 3319–22
- [79] Majkic G, Galstyan E and Selvamanickam V 2015 IEEE Trans. Appl. Supercond. 25 6605304
- [80] Hytch M J and Potez L 1997 Phil. Mag. A 76 1119-38
- [81] Chang W 2019 Comput. Mater. Sci. 164 153-7
- [82] Cantoni C, Gao Y F, Wee S H, Specht E D, Gazquez J, Meng J Y, Pennycook S J and Goyal A 2011 ACS Nano 5 4783–9
- [83] Horide T, Ishimaru M, Sato K and Matsumoto K 2019 Phys. Rev. Mater. 3 013403
- [84] Tarantini C, Jaroszynski J, Kametani F, Zuev Y L, Gurevich A, Chen Y, Selvamanickam V, Larbalestier D C and Christen D K 2011 Phys. Rev. B 84 224514
- [85] Gauquelin N, Zhang H, Zhu G Z, Wei J Y T and Botton G A 2018 AIP Adv. 8 055022
- [86] Khan M Z et al 2019 Sci. Rep. 9 15425
- [87] Jha A K and Matsumoto K 2019 Front. Phys. 7 82
- [88] Galstyan E, Gharahcheshmeh M H, Delgado L, Xu A X, Majkic G and Selvamanickam V 2015 IEEE Trans. Appl. Supercond. 25 5

- [89] Wee S H, Specht E D, Cantoni C, Zuev Y L, Maroni V, Wong-Ng W, Liu G Y, Haugan T J and Goyal A 2011 Phys. Rev. B 83 224520
- [90] Specht E D, Goyal A, Li J, Martin P M, Li X and Rupich M W 2006 Appl. Phys. Lett. 89 162510
- [91] Pinto V, Vannozzi A, Armenio A A, Rizzo F, Masi A, Santoni A, Meledin A, Ferrarese F M, Orlanducci S and Celentano G 2020 Coatings 10 860
- [92] Chen Y, Selvamanickam V, Zhang Y, Zuev Y, Cantoni C, Specht E, Paranthaman M P, Aytug T, Goyal A and Lee D 2009 Appl. Phys. Lett. 94 062513
- [93] Braccini V et al 2011 Supercond. Sci. Technol. 24 035001
- [94] Fujita S, Muto S, Hirata W, Yoshida T, Kakimoto K, Iijima Y, Daibo M, Kiss T, Okada T and Awaji S 2019 IEEE Trans. Appl. Supercond. 29 8001505
- [95] Calderon-Moreno J M 2002 Solid State Ion. 154 125-33
- [96] Gan L, Park Y-J, Kim H, Kim J-M, Ko J-W and Lee J-W 2015 Ceram. Int. 41 9622–7
- [97] Park J S, Kim Y-B, An J, Shim J H, Gur T M and Prinz F B 2013 Thin Solid Films 539 166–9

- [98] Hoedl M F, Makagon E, Lubomirsky I, Merkle R, Kotomin E A and Maier J 2018 Acta Mater. 160 247–56
- [99] Gilardi E, Fabbri E, Bi L, Rupp J L M, Lippert T, Pergolesi D and Traversa E 2017 J. Phys. Chem. C 121 9739–47
- [100] Bjorketun M E, Sundell P G and Wahnstrom G 2007 Phys. Rev. B 76 054307
- [101] Lebedev A I and Sluchinskaya I A 2013 Phys. Solid State 55 1941–5
- [102] Raiteri P, Gale J D and Bussi G 2011 *J. Phys. Condens. Matter* **23** 334213
- [103] Imai G, Nakamura T and Amezawa K 2017 *Solid State Ion.* **303** 12–15
- [104] Babilo P, Uda T and Haile S M 2007 *J. Mater. Res.* **22** 1322–30
- [105] Bendjeriou-Sedjerari B, Loricourt J, Goeuriot D and Goeuriot P 2011 J. Alloys Compd. 509 6175–83
- [106] Yamazaki Y, Yang C-K and Haile S M 2011 *Scr. Mater.* **65** 102–7